The structure and phase transition of tris(*n*-propylammonium) enneachlorodiantimonate (III), $(n-C_3H_7NH_3)_3Sb_2Cl_9$

1996 J. Phys.: Condens. Matter 8 1957

(http://iopscience.iop.org/0953-8984/8/12/010)

J. Phys.: Condens. Matter **8** (1996) 1957–1970. Printed in the UK

The structure and phase transition of tris(*n*-propylammonium) enneachlorodiantimonate (III), $(n\text{-}C_3H_7NH_3)_3Sb_2Cl_9$

P Ciąpała†, J Zaleski‡, G Bator†, R Jakubas† and A Pietraszko§

† Institute of Chemistry, University of Wrocław, 50-383 Wrocław, Joliot Curie 14, Poland
‡ Institute of Chemistry, University of Opole, 45-951 Opole, Oleska 48, Poland
§ Institute of Low Temperature and Structure Research of the Polish Academy of Science (PAS), Okólna 2, 50-422 Wrocław, Poland

Received 4 September 1995, in final form 24 October 1995

Abstract. The crystal structure of $(n\text{-}C_3H_7NH_3)_3Sb_2Cl_9$ at 298 K has been determined (monoclinic, space group Cc, $a = 19.464(2)$ Å, $b = 17.736(2)$ Å, $c = 8.116(2)$ Å, $\beta = 92.81(1)^\circ$, $Z = 4$). The structure consists of one-dimensional polyanionic $(Sb_2Cl_9^{3-})_n$ chains extended along the c-axis, and n-propylammonium cations located in elongated cavities formed by polyanions. The cations are connected to chlorine atoms by N–H···Cl hydrogen bonds. Differential scanning calorimetry, the temperature dependence of the lattice parameters and static electric permittivity studies revealed a first-order phase transition at $T_c = 232$ K of an 'order–disorder' type. It is related to the ordering of n-propylammonium cations that occurs on decreasing the temperature. Debye-like dispersion of the electric permittivity between 30 MHz and 900 MHz is observed over a wide temperature range above T_c. The activation energy of the reorientation of the n-propylammonium cations is found to be 0.29 eV.

1. Introduction

In a reaction of amine hydrochloride and antimony trichloride or bismuth trichloride in solution in an appropriate acid one may obtain salts of a general formula $R_xM_yCl_{x+3y}$ (R is an alkylammonium cation, M is Sb or Bi). Depending on the type of cation and by varying the ratio of reactants used it is possible to obtain one or more products. Among salts that it is potentially possible to obtain, the most common are those of the following formulae: $RMCl_4$, $R_3M_2Cl_9$, R_2MCl_5, and R_3MCl_6 [1–8]. They are molecular ionic salts with anionic sublattices built up of distorted MCl_6^{3-} octahedra, isolated or connected with each other by corners, edges or faces. Alkylammonium cations are located in cavities formed by anionic sublattices and are connected to the chlorine atoms by electrostatic forces and N–H···Cl hydrogen bonds.

Although these salts have been known of for more than a century, only recently have their physical properties been studied. In particular, salts of the general formula $R_3M_2Cl_9$ attract considerable attention, since most of these compounds exhibit a rich structural phase transition sequence, some of the transitions being to polar (ferroelectric or pyroelectric) phases [8–10]. The phase transitions are related to the dynamics of the cationic sublattices. At room temperature the cations usually possess considerable freedom for reorientations, which are the frozen in at transitions to low-temperature phases.

0953-8984/96/121957+14$19.50

In this work we present the crystal structure and results of dilatometric, differential scanning calorimetry (DSC) and dielectric measurements for $(n\text{-}C_3H_7NH_3)_3Sb_2Cl_9$ around the phase transition ($T_c = 232$ K). The results of studies on the synthesis of alkylammonium chloroantimonates and bismuthates for cations differing as regards the length of the *n*-alkyl chains (methyl-, ethyl-, *n*-propyl- and *n*-butylammonium) are also described.

2. Experimental details

The synthesis of chloroantimonate and bismuthate salts was carried out in aqueous solution, with the addition of hydrochloric acid to prevent hydrolysis, by varying the ratio of antimony trichloride (bismuth trichloride) to the appropriate amine hydrochloride from 0.5:1 to 5:1. The salts obtained were dried and characterized by elemental analysis. Single crystals of $(n\text{-}C_3H_7NH_3)_3Sb_2Cl_9$ were grown from an aqueous solution at constant room temperature.

Linear thermal expansion was measured using a thermomechanical analyser—Perkin–Elmer TMS-2. The samples used in the measurements were prepared in the form of thin plates ($5 \times 5 \times 1.5$ mm^3). The anomalies in the vicinity of T_c were always reproducible within 10% for each sample during different runs. The accuracy of the thermal expansion determination was about 3%.

Differential scanning calorimetry (DSC) measurements were carried out on a Perkin–Elmer DSC-7 calorimeter with a heating/cooling rate of 10 K min^{-1}.

For dielectric measurements, samples were cut perpendicularly to the *a*-axis and had dimensions of about $8 \times 2 \times 0.5$ mm^3 ($c \times b \times a$). The plates were silver painted. The complex electric permittivity, $\varepsilon^* = \varepsilon' - i\varepsilon''$, was measured by a HP 4284A Precision LCR Meter in the frequency range from 500 Hz to 1 MHz and a HP 4191A Impedance Analyzer in the frequency range from 30 MHz to 900 MHz. The measurements were performed in the temperature range 200–300 K. The temperature of the specimen was varied continuously at a rate of 0.1 K min^{-1} in the vicinity of T_c and 0.5 K min^{-1} elsewhere in the low-frequency region. In the high-frequency region the temperature was stabilized and controlled by a UNIPAN Temperature Controller, type 650, with fluctuation less than ± 0.1 K. The overall error for the real part of the complex electric permittivity in the low- and high-frequency regions was less than 5% and 10%, respectively.

Data for the structure determination was collected on a KM-4 KUMA diffractometer with Mo Kα radiation ($\lambda = 0.710\,73$ Å, graphite monochromator). Lattice parameters were refined from setting angles of 23 reflections in the $19^\circ < 2\theta < 28^\circ$ range. A summary of the crystal data is presented in table 1. A total of 8336 reflections with $2^\circ < 2\theta < 50^\circ$ were collected using the ω–θ scan technique (scan speed 0.1 deg s^{-1}; scan width 1.0°) of which 2423 had $|F_o| > 4\sigma(|F_o|)$ and were used for structure determination. Two control reflections measured after an interval of 50 reflections showed that the intensity variation was negligible.

Lorentz and polarization measurements with semi-empirical absorption corrections ($\mu_{Mo\ K\alpha} = 28.1$ cm^{-1}) were applied (trans$_{min} = 0.234$, trans$_{max} = 0.328$). The SHELXTL PC program [11] was used for all of the structure calculations and diagrams. The temperature dependences of the lattice parameters was measured on an automatic x-ray diffractometer, type KM4-Bond [12]. The samples used for x-ray measurements were of size $0.6 \times 0.8 \times 0.6$ mm^3. The Bragg 2θ angles $>150^\circ$ were measured for (4 6 9), (−2 14 8), (−18 6 5), (−18 0 −6), (−24 0 2) reflections on cooling in the temperature range 170–290 K using Cu K$\alpha_{1,2}$ radiation.

Table 1. Crystallographic data for (n-$C_3H_7NH_3$)$_3Sb_2Cl_9$.

Unit-cell dimensions:	$a = 19.464(2)$ Å
	$b = 17.736(2)$ Å
	$c = 8.116(2)$ Å
	$\beta = 92.81(1)^\circ$
V	2798(1) Å
Z	4
Formula weight	742.8
Space group	Cc (No 9)
Temperature	25 °C
λ	0.710 73 Å
ρ_{obs}	1.76(1) g cm^{-3}
ρ_{calc}	1.763 g cm^{-3}
μ	2.81 mm^{-1}
$R(F_0)$	3.53%
$R_w(F_0)$	2.78%

$$R = \sum |F(\text{obs}) - F(\text{calc})| \Big/ \sum (F(\text{obs}))$$

$$R_w = \sum \left| F(\text{obs}) - F(\text{calc})\sqrt{\text{weight}} \right| \Big/ \sum \left(F(\text{obs})\sqrt{\text{weight}} \right)$$

Table 2. Possible stoichiometries of alkylammonium chloroantimonates and bismuthates obtained in water solutions by varying the ratio of MCl_3 (M is Sb or Bi) to the appropriate alkylammonium chloride (asterisks indicate salts reported earlier that we were able to synthesize).

R = cation	$RSbCl_4$	$R_3Sb_2Cl_9$	R_2SbCl_5	R_3SbCl_6	Other
$CH_3NH_3^+$	—	[1, 2, 3]*	—	—	R_2SbCl_5·RCl [1, 4]*
$C_2H_5NH_3^+$	[1]*	—	—	[1, 3]*	
$C_3H_7NH_3^+$	—	Present work	[3]*	—	
$C_4H_9NH_3^+$	—	—	Present work	Present work	
R = cation	$RBiCl_4$	$R_3Bi_2Cl_9$	R_2BiCl_5	R_3BiCl_6	Other
$CH_3NH_3^+$	—	[5, 6]*	—	—	R_3BiCl_6·RCl [5]*
					$R_5Bi_2Cl_{11}$ [5, 7]*
$C_2H_5NH_3^+$	[5]	—	[5]*	[6]	R_3BiCl_6·RCl [5]
$C_3H_7NH_3^+$	[5]	—	[5]*	—	R_3BiCl_6·RCl [5]*
$C_4H_9NH_3^+$	—	—	[5]*	—	R_3BiCl_6·3RCl [5]

3. Results and discussion

3.1. Synthesis of alkylammonium chloroantimonates (III) and chlorobismuthates (III)

The results of synthetic studies as well as literature results are presented in table 2. Elemental analysis for the new crystals gave the following results (the values in brackets are theoretical compositions, all values are in weight per cent): (i) (n-$C_3H_7NH_3$)$_3Sb_2Cl_9$, C, 14.55 (14.54); H, 4.21 (4.07); N, 5.58 (5.65); (ii) (n-$C_4H_9NH_3$)$_2SbCl_5$, C, 21.26 (21.48); H, 5.57 (5.41); N, 6.14 (6.26); (iii) (n-$C_4H_9NH_3$)$_3SbCl_6$, C, 25.97 (25.88); H, 6.83 (6.52); N, 7.32(7.55).

On increasing the length of the alkyl chain of the cation the salts tend to crystallize in one of two stoichiometries, R_2MX_5 and R_3MX_6 (or $R_3MX_6 \cdot RX$). This may be rationalized by taking into account steric effects, which lead to structures built up of small (in spatial dimensions) anions. In the case of R_3MX_6 (or $R_3MX_6 \cdot RCl$) they are built up of isolated MX_6^{3-} octahedra (or isolated MX_6^{3-} octahedra and Cl^- ions [13]). In the case of R_2MX_5

stoichiometry either of MX_5^{2-} square pyramids [14] or isolated $M_2X_{10}^{4-}$ units composed of two octahedra sharing an edge occur [15].

Among all the salts obtained there is one new compound of $R_3M_2X_9$ stoichiometry, namely $(n\text{-}C_3H_7NH_3)_3Sb_2Cl_9$. Since compounds of such stoichiometry possess the most interesting properties we decided to study its structure and properties by x-ray diffraction, DSC, dielectric and dilatometric methods.

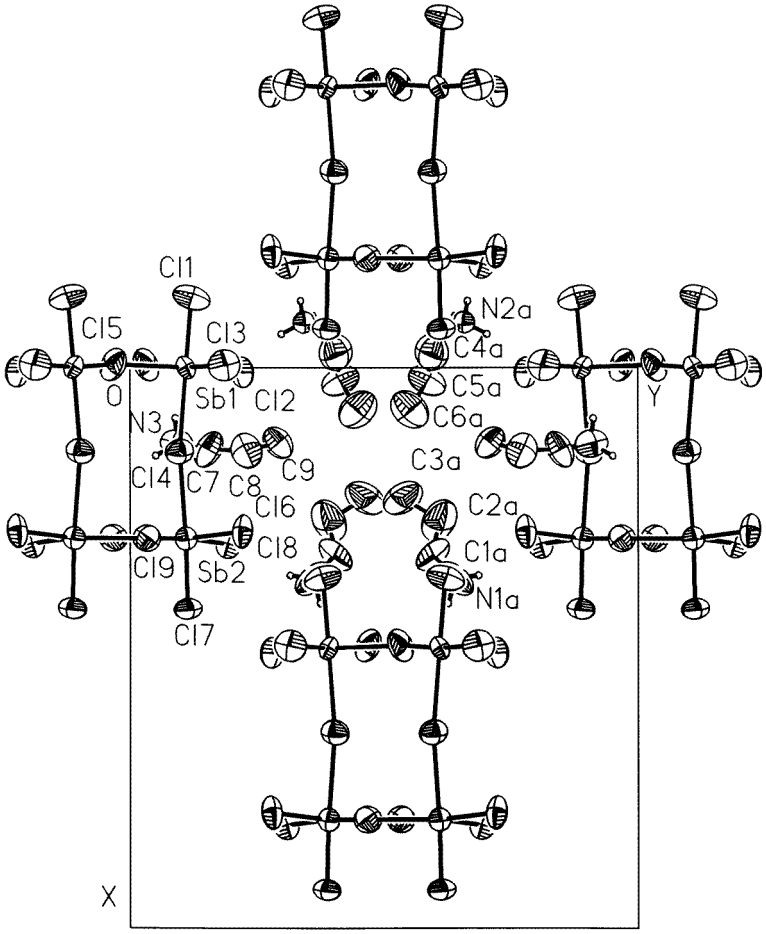

Figure 1. Projection of the crystal structure of $(n\text{-}C_3H_7NH_3)_3Sb_2Cl_9$ on the ***a*–*b*** plane.

3.2. The structure and phase transition of n-propylammonium enneachlorodiantimonate

3.2.1. X-rays. From the systematic absences, the non-centrosymmetrical *Cc* or centrosymmetrical $C2/c$ space group is indicated. Solution in the $C2/c$ group was unsuccessful, so the *Cc* space group was chosen. The structure was solved by the Patterson method and subsequent difference Fourier synthesis. It was refined in the full-matrix least-squares method using anisotropic temperature factors. Hydrogen atoms connected to the nitrogen atoms were placed from geometric considerations, and were not refined. The *n*-propylammonium cations are characterized by large thermal motions which are reflected in

Table 3. Atomic coordinates (in units of 10^4) and equivalent isotropic displacement coefficients of refined atoms of (n-$C_3H_7NH_3$)$_3Sb_2Cl_9$ at 298 K (10^3 Å^2). The equivalent isotropic U is defined as one third of the trace of the orthogonalized U_{ij}-tensor.

Sb(1)	0	1095	0	55(1)
Sb(2)	3050(1)	1093(1)	824(1)	59(1)
Cl(1)	−1246(4)	1208(5)	−256(11)	121(2)
Cl(2)	82(4)	2213(4)	−1676(9)	83(2)
Cl(3)	−42(5)	1850(5)	2589(11)	106(2)
Cl(4)	1499(6)	968(1)	547(13)	88(1)
Cl(5)	−47(5)	−320(5)	2049(11)	109(2)
Cl(6)	2922(4)	2214(4)	2487(9)	92(2)
Cl(7)	4306(3)	1128(4)	1227(9)	79(2)
Cl(8)	3145(4)	1937(4)	−1640(9)	81(2)
Cl(9)	3046(4)	328(5)	3841(11)	97(2)
N(1)	8762(9)	1405(8)	5137(19)	144(3)
C(1)	8335(12)	959(11)	4870(24)	156(3)
C(2)	7722(12)	1085(11)	4177(28)	204(3)
C(3)	7322(11)	373(13)	4128(22)	170(3)
N(2)	4186(5)	1581(5)	5408(12)	54(2)
C(4)	4724(12)	947(12)	6849(24)	158(3)
C(5)	5237(10)	855(10)	5657(19)	138(3)
C(6)	5743(12)	511(12)	7473(22)	171(3)
N(3)	1356(5)	920(5)	4626(11)	108(3)
C(7)	1458(15)	1544(8)	5347(34)	128(3)
C(8)	1481(12)	2294(8)	5787(23)	138(3)
C(9)	1337(8)	2913(7)	5035(23)	147(3)

Symmetry code:

None:	x	y	z	(iv)	$-\frac{1}{2}+x$	$\frac{1}{2}-y$	$\frac{1}{2}+z$
(i)	x	$-y$	$\frac{1}{2}+z$	(v)	$-\frac{1}{2}+x$	$\frac{1}{2}+y$	z
(ii)	$\frac{1}{2}+x$	$\frac{1}{2}+y$	z	(vi)	x	$1-y$	$\frac{1}{2}+z$
(iii)	$\frac{1}{2}+x$	$\frac{1}{2}-y$	$\frac{1}{2}+z$	(vii)	x	$1+y$	z

their large temperature factors. Attempts to split positions of carbon atoms by assuming various models of the disorder of the cations were, however, not successful. The positional parameters of non-hydrogen atoms are presented in table 3. The anionic sublattice of (n-$C_3H_7NH_3$)$_3Sb_2Cl_9$ crystal is composed of one-dimensional polyanionic $(Sb_2Cl_9^{3-})_n$ chains composed of $SbCl_6^{3-}$ octahedra, connected with each other by corners, extended along the c-axis. They form cavities where three non-equivalent n-propylammonium cations are located. The cations are connected to the anionic sublattice by electrostatic interactions and N–H$\cdots$Cl hydrogen bonds. It should be noted that the cations are located in cavities in such a way that all of the alkyl chains are directed toward the centre of the cavity and the N atoms are facing to the outside of it. The shortest N$\cdots$Cl contacts in (n-$C_3H_7NH_3$)$_3Sb_2Cl_9$ are 3.28–3.46 Å; this range corresponds to moderately strong hydrogen bonds. A projection of the crystal structure of (n-$C_3H_7NH_3$)$_3Sb_2Cl_9$ onto the $\boldsymbol{a}$–$\boldsymbol{b}$ plane showing the atomic numbering scheme is presented in figure 1. Selected bond distances and angles of (n-$C_3H_7NH_3$)$_3Sb_2Cl_9$ are given in table 4. The antimony atoms are at the centres of distorted octahedra with three short Sb–Cl bonds in the range from 2.41 to 2.51 Å and three long ones in the range from 2.76 to 3.03 Å. Each short bond is opposite to a long one. The bond angles of the anion are in the range 84.6–95.6°. The lengths and angles of the cations are

Table 4. Selected bond distances (Å) and angles (deg) of $(n\text{-}C_3H_7NH_3)_3Sb_2Cl_9$ at 298 K.

Sb(1)–Cl(1)	2.433 (8)	Cl(1)–Sb(1)–Cl(5A)	88.7(3)
Sb(1)–Cl(2)	2.414 (7)	Cl(2)–Sb(1)–Cl(3)	92.3(3)
Sb(1)–Cl(3)	2.497 (9)	Cl(2)–Sb(1)–Cl(4)	93.2(2)
Sb(1)–Cl(4)	2.938 (12)	Cl(2)–Sb(1)–Cl(5)	177.7(3)
Sb(1)–Cl(5)	3.014 (8)	Cl(2)–Sb(1)–Cl(5A)	85.4(2)
Sb(1)–Cl(5A)	2.760 (9)	Cl(3)–Sb(1)–Cl(4)	89.2(3)
Sb(2)–Cl(4)	3.025 (12)	Cl(3)–Sb(1)–Cl(5)	88.8(3)
Sb(2)–Cl(6)	2.423 (8)	Cl(3)–Sb(1)–Cl(5A)	175.5(3)
Sb(2)–Cl(7)	2.451 (7)	Cl(4)–Sb(1)–Cl(5)	84.8(2)
Sb(2)–Cl(8)	2.512 (7)	Cl(4)–Sb(1)–Cl(5A)	94.8(3)
Sb(2)–Cl(9)	2.800 (9)	Cl(5)–Sb(1)–Cl(5A)	93.6(1)
Sb(2)–Cl(9A)	2.989 (8)	Cl(4)–Sb(2)–Cl(6)	88.4(2)
		Cl(4)–Sb(2)–Cl(7)	175.6(2)
		Cl(4)–Sb(2)–Cl(8)	95.6(2)
		Cl(4)–Sb(2)–Cl(9)	89.1(2)
		Cl(4)–Sb(2)–Cl(9A)	85.5(2)
		Cl(6)–Sb(2)–Cl(7)	91.9(3)
		Cl(6)–Sb(2)–Cl(8)	88.1(2)
		Cl(6)–Sb(2)–Cl(9)	84.6(2)
		Cl(6)–Sb(2)–Cl(9A)	173.7(2)
		Cl(7)–Sb(2)–Cl(8)	88.8(3)
		Cl(7)–Sb(2)–Cl(9)	86.6(2)
		Cl(7)–Sb(2)–Cl(9A)	94.0(2)
		Cl(8)–Sb(2)–Cl(9)	171.3(2)
		Cl(8)–Sb(2)–Cl(9A)	94.1(2)
		Cl(9)–Sb(2)–Cl(9A)	93.6(1)
		Sb(1)–Cl(4)–Sb(2)	170.3(2)
		Sb(1)–Cl(5)–Sb(1A)	153.3(3)
		Sb(2)–Cl(9)–Sb(2A)	151.5(3)

not listed in table 4 since they are determined with lower accuracy because of their large thermal motions.

Table 5. The changes of the linear thermal expansion along the *a*-, *b*- and *c*-axes at T_c, the transition volume, and the pressure coefficient (dT_c/dp) for $(n\text{-}C_3H_7NH_3)_3Sb_2Cl_9$.

Axis	$10^3\Delta L/L$	$10^3\Delta V/V$	dT_c/dp (10^{-2} K MPa^{-1})
a	−0.6		
b	+2.5	−0.35	−4.5
c	−2.25		

3.2.2. Dilatometric measurements. Figure 2 shows the thermal expansion of $(n\text{-}C_3H_7NH_3)_3Sb_2Cl_9$ along the *a*-, *b*- and *c*-axes, on heating. A clear sharp anomaly at 233 K indicates a discontinuous character of the structural phase transition. At the phase transition point one can see a distinct contraction along the *b*-axis and dilation along the *c*- and *a*-axes with decreasing temperature. Above T_c, a crystal of $(n\text{-}C_3H_7NH_3)_3Sb_2Cl_9$ expands linearly with the positive thermal expansion coefficients: $\bar{\alpha}_c = 3.1\times10^{-5}$ K^{-1}, $\bar{\alpha}_b = 4.8\times10^{-5}$ K^{-1}, $\bar{\alpha}_a = 1.4\times10^{-4}$ K^{-1} (the mean value of α is defined as $(L_1-L_2)/[L_{(300\ \mathrm{K})}(T_1-T_2)]$). Below T_c a strong non-linearity in $\Delta L/L_0$ is observed especially along the *a*- and *c*-axes. Table 5

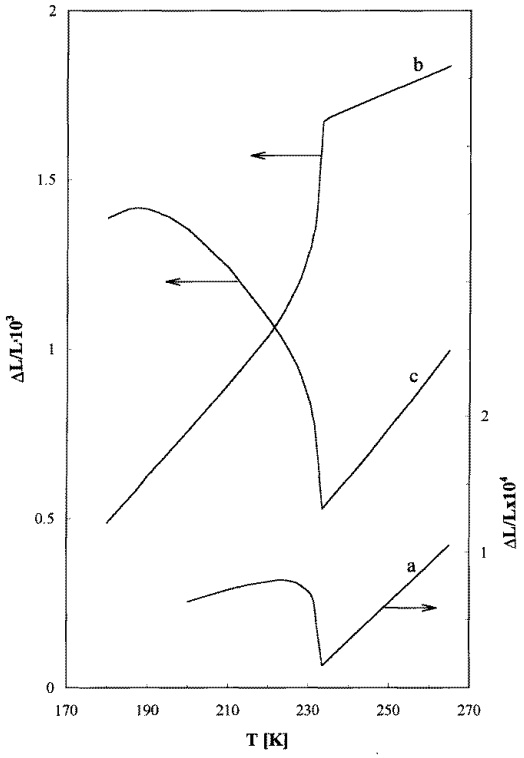

Figure 2. The temperature dependence of the linear thermal expansion $\Delta L/L$ of (n-$C_3H_7NH_3)_3Sb_2Cl_9$ crystal along the a-, b- and c-axes.

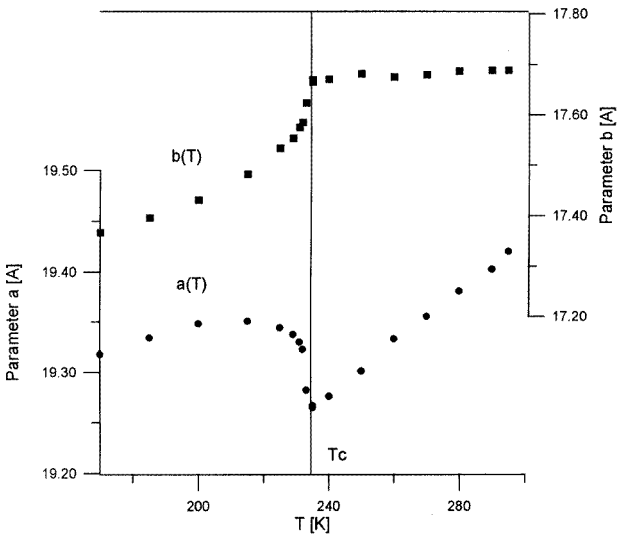

Figure 3. The experimental values of the lattice parameters a and c as functions of the temperature for (n-$C_3H_7NH_3)_3Sb_2Cl_9$ crystal.

shows the size of the anomaly in the linear thermal expansion of the $(n\text{-}C_3H_7NH_3)_3Sb_2Cl_9$ at the phase transition temperature along the main crystallographic directions calculated from the dilatometric measurements. The pressure coefficient of the transition temperature can be estimated from the Clausius–Clapeyron relation: $dT_c/dp = \Delta V/\Delta S$, where ΔV is the change in molar volume and ΔS is the entropy change corresponding to the latent heat at T_c.

3.2.3. Thermal expansion studied with x-rays. The temperature dependence of the lattice parameters confirms the presence of the structural phase transition. The *b*- and *a*-parameters both have distinct steps at about 232 K, on cooling (see figure 3). Figure 4 shows the variations of the *c*-parameter and the monoclinic angle (β) with temperature. We should note that β reveals only a continuous change of slope at the phase transition. The x-ray temperature studies showed that the symmetry of the $(n\text{-}C_3H_7NH_3)_3Sb_2Cl_9$ crystal decreases from monoclinic to triclinic. This was confirmed by the splitting of reflections below T_c. It suggests the presence of a ferroelastic phase below 232 K.

3.2.4. Differential scanning calorimetry (DSC). The DSC plot (see figure 5) for the temperature range 215–245 K revealed one distinct thermal anomaly at 232 K on heating (231 K on cooling), that is both perfectly reproducible and reversible. It should be noticed that this transition appears to have a C_p-'tail' stretching back to 215 K. This suggests that the first-order transition of the order–disorder type also has some features of a transition of a second-order type. The transition enthalpy and entropy determined on heating from the peak area are $\Delta H_{tr} = 1.06$ J g^{-1}, and $\Delta S_{tr} = 3.5$ J mol^{-1} K^{-1}, respectively.

3.2.5. Dielectric studies. Since we were not able to prepare a large single crystal of $(n\text{-}C_3H_7NH_3)_3Sb_2Cl_9$, the dielectric measurements were performed only for plates cut perpendicularly to the *a*-axis. The temperature dependence of the real part (ε'_a) of the

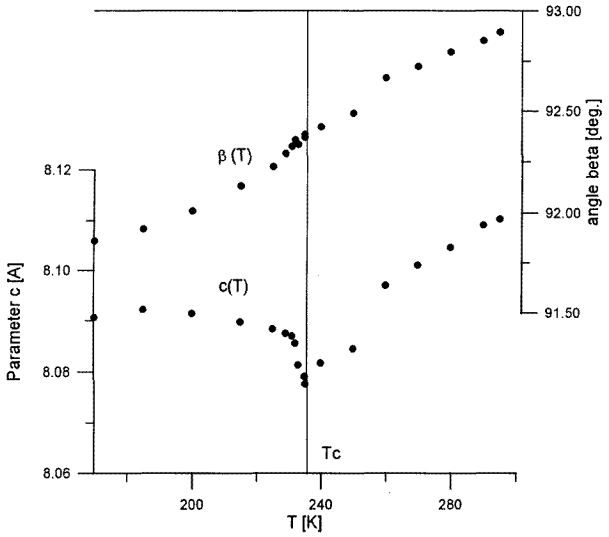

Figure 4. The experimental values of the lattice parameter *c* and the monoclinic angle β as functions of the temperature for $(n\text{-}C_3H_7NH_3)_3Sb_2Cl_9$ crystal.

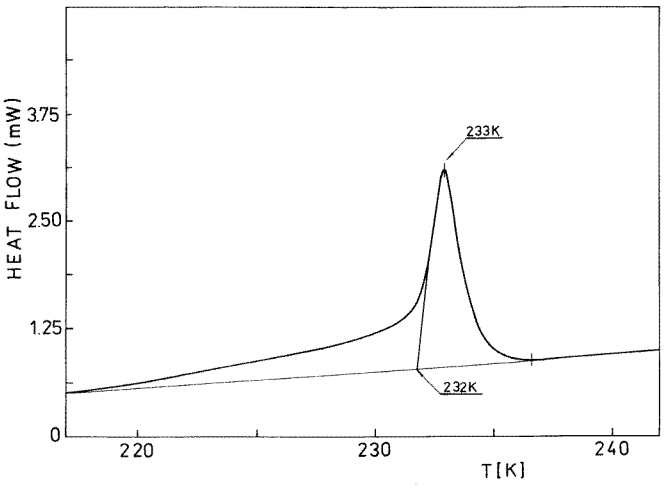

Figure 5. DSC measurements for $(n\text{-}C_3H_7NH_3)_3Sb_2Cl_9$ (sample mass = 19.5 mg, scanning rate = 10 K min^{-1}, on heating).

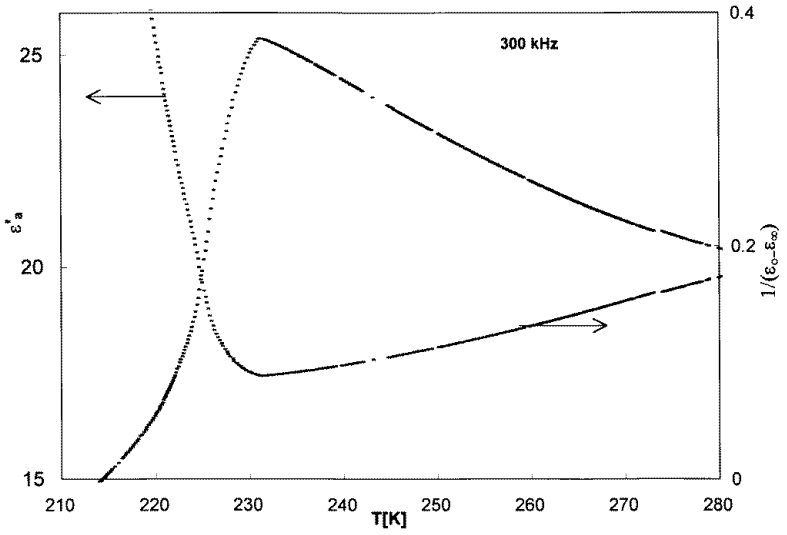

Figure 6. The temperature dependence of the real part of the complex electric permittivity, ε'_a, at 300 kHz and the inverse of the electric permittivity, $1/\varepsilon_a$, for $(n\text{-}C_3H_7NH_3)_3Sb_2Cl_9$, on cooling.

complex electric permittivity (ε^*) measured at 300 kHz in the temperature range 210–280 K is shown in figure 6. A plot of the imaginary part of ε^*_a as a function of temperature is presented in figure 7. For the sake of clarity only the electric permittivity measured at 30 kHz, 300 kHz and 1 MHz is shown. The electric permittivity, ε'_a, increases linearly with temperature reaching a maximum (26 units) at 232 K, which agrees well with the transition temperature detected by DSC and dilatometric measurements. Below this point a rapid change in the slope of the $\varepsilon'(T)$-curve is observed. The temperature behaviour of ε'_a indicates that the structural phase transition exhibits features of both first- and second-

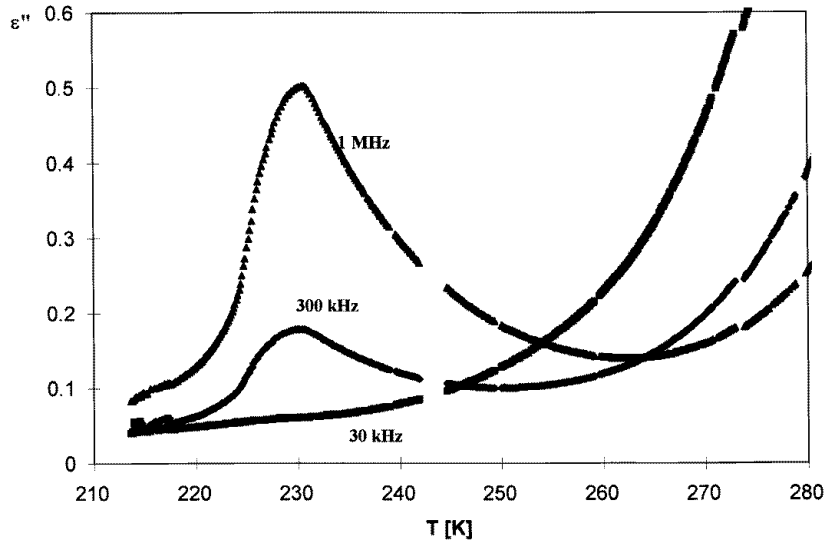

Figure 7. The temperature dependence of the imaginary part of the complex electric permittivity, ε_a'', at 30 kHz, 300 kHz and 1 MHz.

order type. Within experimental accuracy, the transition point seems to occur at the same temperature $T_c = 232$ K, irrespective of the measuring frequency between 1 kHz and 1 MHz. ε_a' measured at 300 kHz can be taken as the static electric constant ε_0. The electric permittivity along the a-axis on the high-temperature side of T_c can be well expressed by the Curie–Weiss law (figure 6):

$$\varepsilon = \frac{c}{T - T_0}$$

with the fitting parameter $C = 644$ K and $T_0 = 177$ K. The dielectric measurements performed in a microwave frequency region, 30 MHz–900 MHz, clearly indicate the presence of a relaxation process in the high-temperature phase (see figure 8). The Cole–Cole diagrams for the electric permittivity along the a-axis obtained at several temperatures are shown in figure 9, indicating that the dielectric dispersion can be well described by the formula

$$\varepsilon^*(\omega) = \varepsilon_\infty + \frac{\varepsilon_0 - \varepsilon_\infty}{1 + (\mathrm{i}\omega\tau)^{1-\alpha}}$$

where ε_0 and ε_∞ are the low- and high-frequency limits of the electric permittivity, respectively, ω is the angular frequency, τ is the macroscopic relaxation time and the α-parameter represents a measure of the width of the distribution of the relaxation time. The values of the α-parameter estimated by least-squares fitting vary from 0.01 to 0.1 in the temperature range from 260 to 232 K. It should, however, be stressed that a small asymmetry visible at the high-frequency end of the Cole–Cole plots suggests the possibility of the appearance of an additional higher-frequency relaxator.

The value of τ as a function of temperature and $\lg \tau$ as a function of inverse temperature obtained for the main dispersion above T_c are shown in figure 10. The activation energy of the thermally activated process calculated from the plot of $\ln \tau = f(1/T)$ amounts to 0.29 eV. Because of polydispersive behaviour, the true activation energy may differ from the value given above by $\sim$10% .

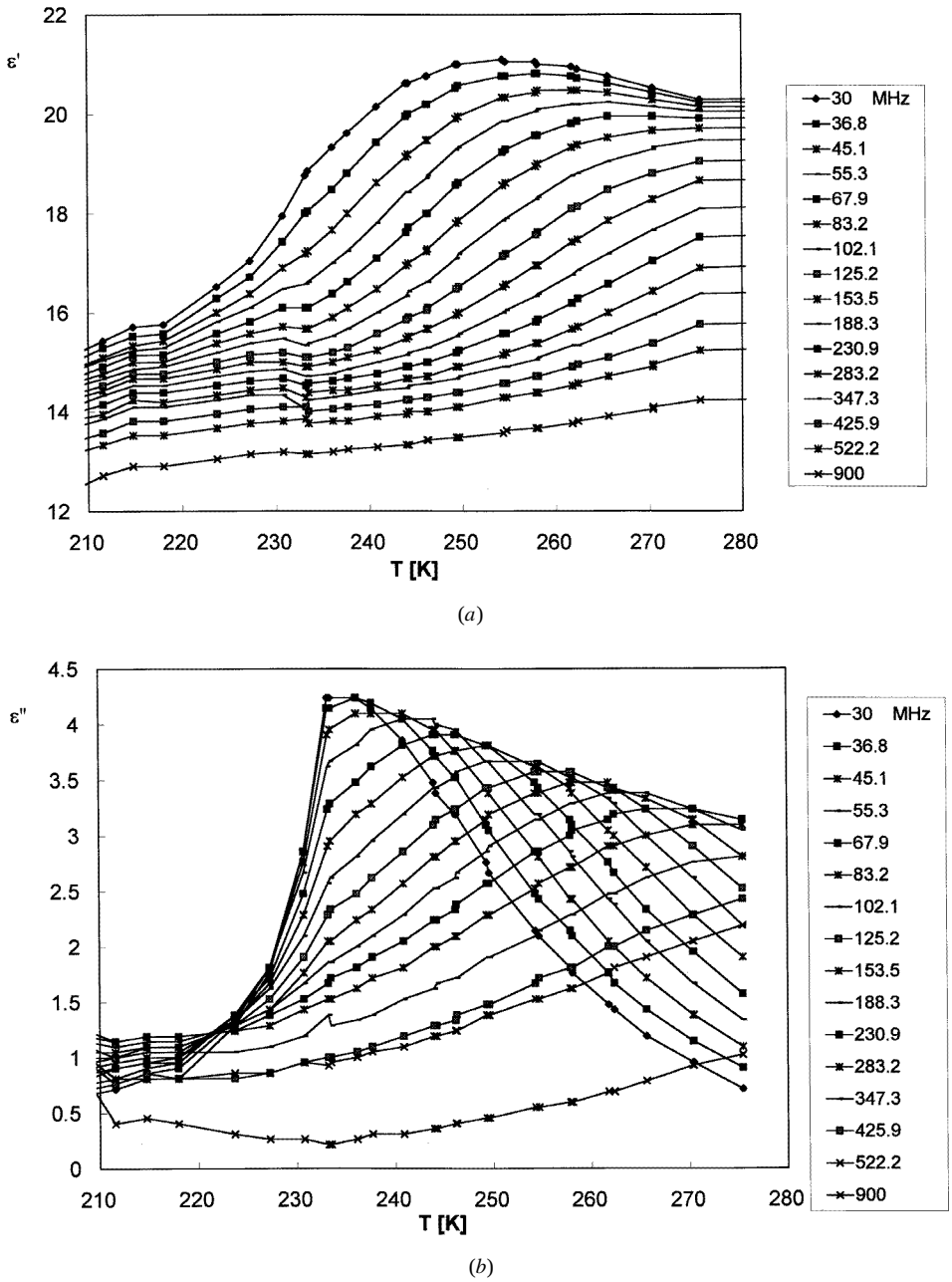

Figure 8. The temperature dependence of the real (*a*) and imaginary (*b*) parts of the complex electric permittivity at frequencies from 30 to 900 MHz, on cooling.

It is difficult to discuss the dielectric anisotropy in this crystal since the measurements were performed only for the *a*-direction. However, the electric permittivity of a polycrystalline sample measured at 100 kHz shows a broad maximum with $\varepsilon_{max} = 10$ at 232 K. This indicates the existence of anisotropy of dielectric properties, since this value is

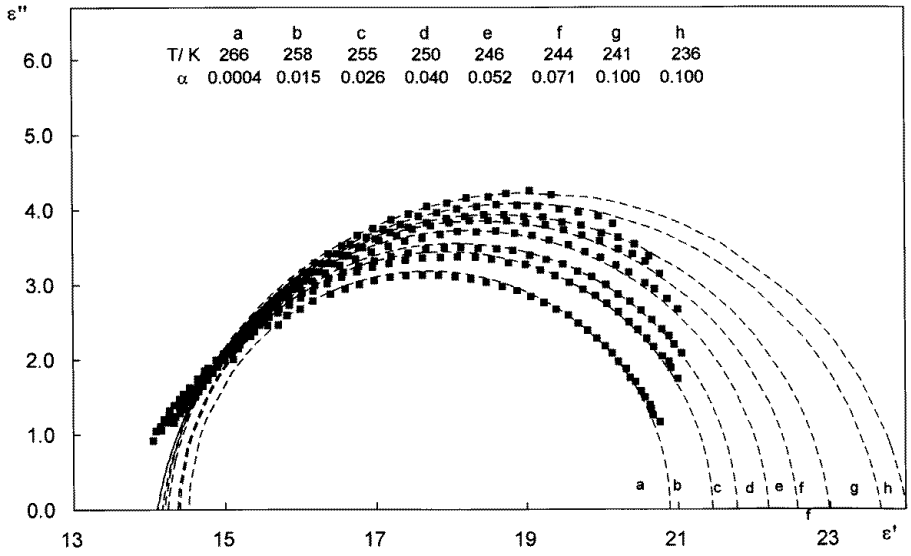

Figure 9. Cole–Cole diagrams of the electric permittivity measured along the *a*-axis in the frequency range from 30 to 450 MHz.

markedly lower than that obtained for a single-crystal sample and suggests that the largest effect probably appears along the *a*-axis.

4. General discussion

The x-ray studies of $(n\text{-}C_3H_7NH_3)_3Sb_2Cl_9$ showed that the *n*-propylammonium cations appeared to be disordered in the high-temperature phase. This disorder is likely to be dynamical and is suggested to contribute to the phase transition mechanism at 232 K by analogy with corresponding transitions found in similar halogenoantimonate (III) and bismuthate (III) compounds, namely: $(n\text{-}C_3H_7NH_3)_2SbBr_5$ [16, 17] and $(n\text{-}C_3H_7NH_3)_2BiBr_5$ [18]. The NMR measurements on the former crystal [19] showed that *n*-propylammonium cations perform the C_3 type of reorientation of the CH_3 and NH_3^+ groups. At higher temperature a cationic tumbling about its centre of gravity is postulated. The NMR studies in similar *n*-propylammonium crystals showed that the NH_3^+ reorientations persist usually down to about 150–100 K. This means that the movements of NH_3^+ groups do not seem to be affected at the phase transition which takes place at higher temperature (232 K) in the title crystal. Moreover, the C_3 type of reorientation of the NH_3^+ and CH_3 groups does not contribute to the resultant dipole moment, and so the observed change of the electric permittivity at T_c may have its origin in the reorientation of the alkyl chains.

Taking into account the large anisotropic temperature factors of all carbon atoms and nitrogen atoms of *n*-propylammonium cations, we suggest flips of alkyl chains around their long axes. The phase transition is probably due to change in the N–H $\cdots$ Cl hydrogen-bonding system followed by a reorientation of the propylammonium chains. Such a mechanism for phase transitions has been encountered in most of the known *n*-propylammonium crystals of the formula $(RNH_3)_2MX_4$ where R stands for alkyl, M stands for Mn, Cd, Cu, Zn, and X stands for Cl, Br [20–22].

A low value of the macroscopic relaxation time t found in our dielectric measurements

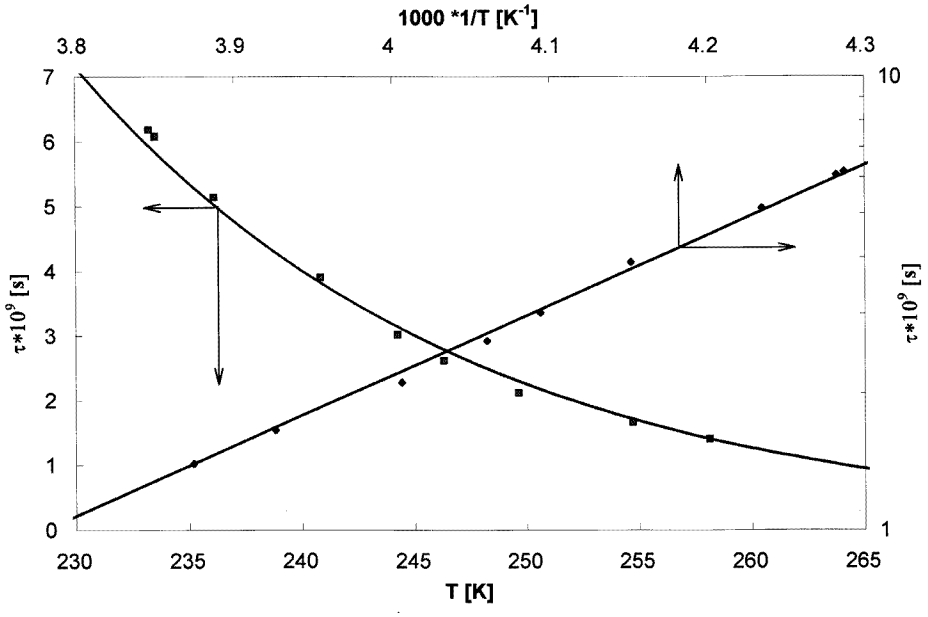

Figure 10. The temperature dependence of the macroscopic relaxation time, τ, and the plot of the Arrhenius relation in the high-temperature phase of $(n\text{-}C_3H_7NH_3)_3Sb_2Cl_9$.

$(6\times10^{-9}$ s at $T_c)$ seems to be consistent with the mechanism of cation reorientation proposed in x-ray studies.

The polar nature of the low-temperature phase (below $T_c = 232$ K) should be excluded since no pyroelectric effect has been observed along the a-axis of $(n\text{-}C_3H_7NH_3)_3Sb_2Cl_9$ crystal in the vicinity of the transition point.

5. Conclusions

X-ray studies showed that the structure of $(n\text{-}C_3H_7NH_3)_3Sb_2Cl_9$ crystal at room temperature consists of one-dimensional polyanionic $(Sb_2Cl_9^{3-})_n$ chains and three non-equivalent n-propylammonium cations. The cations appear to be dynamically disordered. The calorimetric (DSC), dilatometric and lattice parameter measurements showed that $(n\text{-}C_3H_7NH_3)_3Sb_2Cl_9$ undergoes a first-order structural phase transition at 232 K. The analysis of the results for the high-frequency dielectric dispersion (30 MHz–900 MHz) and the temperature behaviour of the static electric permittivity near T_c led us to postulate a hindered rotation or flipping of n-propylammonium cations around their long axes in the high-temperature phase (above 232 K). The mechanism of the phase transition is undoubtedly related to the rapid freezing of such reorientations at T_c. The Curie–Weiss-like behaviour of ε_a over the wide temperature range above T_c points to cooperative interactions between the alkylammonium groups.

Acknowledgment

This work was sponsored in part by the Committee for Scientific Research within the projects 2P 303 040 05 and 3P 40705605.

References

[1] Ensinger U, Schwarz W and Schmidt A Z 1982 *Z. Naturf.* b **37** 1584
[2] Jakubas R, Czapla Z, Galewski Z, Sobczyk L, Żogał O J and Lis T 1986 *Phys. Status Solidi* a **93** 449
[3] Whealy R and Linder D E 1968 *Inorg. Chim. Acta* 49
[4] Ensinger U, Schwarz W and Schmidt A 1983 *Z. Naturf.* b **38** 149
[5] Remy H and Pellens L 1928 *Chem. Ber.* **61** 862
[6] Jakubas R, Tomaszewski P E and Sobczyk L 1989 *Phys. Status Solidi* a **111** K27
[7] Lefebvre J, Carpentier P and Jakubas R 1991 *Acta Crystallogr.* B **47** 228
[8] Jakubas R and Sobczyk L 1990 *Phase Transitions* **20** 163
[9] Varma V, Bhattacharjee R, Vasan H N and Rao C N 1992 *Spectrochim. Acta* A **48** 1631
[10] Ishihara H, Watanabe K, Iwata A, Yamada K, Kinoshita Y, Okuda T, Krishnan V G, Dou S and Weiss A 1992 *Z. Naturf.* a **47** 65
[11] *SHELXTL PC Program System* 1990 Siemens Analytical X-ray Instruments Inc., Madison, WI
[12] Kucharczyk D, Pietraszko A and Łukaszewicz K 1993 *J. Appl. Crystallogr.* **26** 467
[13] Herdtweck E and Kreusel U 1993 *Acta Crystallogr.* C **49** 318
[14] Lipka A 1980 *Z. Anorg. Allg. Chem.* **469** 229
[15] Webster M and Keats S 1971 *J. Chem. Soc.* A 298
[16] Okuda T, Tanaka N, Ichiba S and Yamada K 1986 *Z. Naturf.* a **41** 319
[17] Jakubas R, Bator G, Foulon M, Lefebvre J and Matuszewski J 1992 *Z. Naturf.* a **48** 529
[18] Piślewski N, Tritt-Goc J and Jakubas R 1996 *Solid State NMR* at press
[19] Piślewski N, Tritt-Goc J and Jakubas R 1994 *Solid State NMR* **3** 293
[20] Muralt P and Kind R 1988 *Phys. Rev.* B **38** 666
[21] Doudin B and Chapuis G 1990 *Acta Crystallogr.* B **46** 175
[22] Zoniga F J, Tello M J, Perez-Mato J M and Perez-Jubindo M A 1982 *J. Chem. Phys.* **76** 2610